

The metal grating design of plasmonic hybrid III-V/Si evanescent lasers

Min-Hsiang Hsu,¹ Chien-Chung Lin,^{1,*} and Hao-Chung Kuo²

¹Institute of Photonic System, National Chiao Tung University, Tainan 711, Taiwan

²Department of Photonics and Institute of Electro-Optical Engineering, National Chiao Tung University, Hsinchu 30010, Taiwan

*chienchunglin@faculty.nctu.edu.tw

Abstract: A hybrid III-V/silicon laser design with a metal grating layer inserted in between is proposed and numerically studied. The metal grating layer is buried in a silicon ridge waveguide surrounded by silicon dioxide, and its structural parameters such as periodicity, width and depth can be varied for optimization purpose. The plasmonic effect originated from the grating layer can manage optical fields between III-V and silicon layers in hopes of dimension reduction. The substrate is planarized to minimize the bonding failure. A numerical algorithm with various combinations of metal grating and waveguide structural parameters was created and the optimal design with 730 nm grating period and 600 nm of buried waveguide ridge height was obtained by minimizing the corresponding laser threshold. With top AlInGaAs quantum wells and optimized design of hybrid metal/silicon waveguide, a $0.6 \mu\text{m}^{-1}$ threshold gain can be achieved.

©2013 Optical Society of America

OCIS codes: (140.5960) Semiconductor lasers; (250.5403) Plasmonics; (230.7370) Waveguides.

References and links

1. R. S. Jacobsen, K. N. Andersen, P. I. Borel, J. Fage-Pedersen, L. H. Frandsen, O. Hansen, M. Kristensen, A. V. Lavrinenko, G. Moulin, H. Ou, C. Peucheret, B. Zsigri, and A. Bjarklev, "Strained silicon as a new electro-optic material," *Nature* **441**(7090), 199–202 (2006).
2. A. Liu, L. Liao, D. Rubin, H. Nguyen, B. Ciftcioglu, Y. Chetrit, N. Izhaky, and M. Paniccia, "High-speed optical modulation based on carrier depletion in a silicon waveguide," *Opt. Express* **15**(2), 660–668 (2007).
3. R. Salem, M. A. Foster, A. C. Turner, D. F. Geraghty, M. Lipson, and A. L. Gaeta, "Signal regeneration using low-power four-wave mixing on silicon chip," *Nat. Photonics* **2**(1), 35–38 (2008).
4. O. Boyraz and B. Jalali, "Demonstration of a silicon Raman laser," *Opt. Express* **12**(21), 5269–5273 (2004).
5. T. J. Kippenberg, J. Kalkman, A. Polman, and K. J. Vahala, "Demonstration of an erbium-doped microdisk laser on a silicon chip," *Phys. Rev. A* **74**(5), 051802 (2006).
6. L. Pavesi, L. Dal Negro, C. Mazzoleni, G. Franzò, and F. Priolo, "Optical gain in silicon nanocrystals," *Nature* **408**(6811), 440–444 (2000).
7. R. Chen, T. T. D. Tran, K. W. Ng, W. S. Ko, L. C. Chuang, F. G. Sedgwick, and C. Chang-Hasnain, "Nanolasers grown on silicon," *Nat. Photonics* **5**(3), 170–175 (2011).
8. A. W. Fang, H. Park, O. Cohen, R. Jones, M. J. Paniccia, and J. E. Bowers, "Electrically pumped hybrid AlGaInAs-silicon evanescent laser," *Opt. Express* **14**(20), 9203–9210 (2006).
9. A. J. Zilkie, P. Seddighian, B. J. Bijlani, W. Qian, D. C. Lee, S. Fatholouloumi, J. Fong, R. Shafiha, D. Feng, B. J. Luff, X. Zheng, J. E. Cunningham, A. V. Krishnamoorthy, and M. Asghari, "Power-efficient III-V/Silicon external cavity DBR lasers," *Opt. Express* **20**(21), 23456–23462 (2012).
10. A. W. Fang, E. Lively, Y. H. Kuo, D. Liang, and J. E. Bowers, "A distributed feedback silicon evanescent laser," *Opt. Express* **16**(7), 4413–4419 (2008).
11. X. Sun, A. Zadok, M. J. Shearn, K. A. Diest, A. Ghaffari, H. A. Atwater, A. Scherer, and A. Yariv, "Electrically pumped hybrid evanescent Si/InGaAsP lasers," *Opt. Lett.* **34**(9), 1345–1347 (2009).
12. D. Liang, G. Roelkens, R. Baets, and J. E. Bowers, "Hybrid Integrated Platforms for Silicon Photonics," *Materials* **3**(3), 1782–1802 (2010).
13. J. Liu, X. Sun, R. Camacho-Aguilera, L. C. Kimerling, and J. Michel, "Ge-on-Si laser operating at room temperature," *Opt. Lett.* **35**(5), 679–681 (2010).
14. W. L. Barnes, A. Dereux, and T. W. Ebbesen, "Surface plasmon subwavelength optics," *Nature* **424**(6950), 824–830 (2003).

15. D. Pasquariello and K. Hjort, "Plasma-assisted InP-to-Si low temperature wafer bonding," *IEEE J. Sel. Top. Quant.* **8**(1), 118–131 (2002).
16. R. F. Oulton, V. J. Sorger, D. A. Genov, D. F. P. Pile, and X. Zhang, "A hybrid plasmonic waveguide for subwavelength confinement and long-range propagation," *Nat. Photonics* **2**(8), 496–500 (2008).
17. L. A. Coldren, S. W. Corzine, and M. L. Masanovic, "Modal gain, modal loss, and confinement factors," in *Diode Lasers and Photonic Integrated Circuits*, K. Chang, ed. (John Wiley & Sons, 2012).
18. M. Bass, C. DeCusatis, J. Enoch, V. Lakshminarayanan, G. Li, C. MacDonald, V. Mahajan, and E. V. Stryland, "Optical properties of materials, nonlinear optics, quantum optics" in *Handbook of Optics third edition*, (McGraw-Hill Professional, New York, 2009).
19. H. Dejun, "Refractive index of AlInGaAs layers in the transparent wavelength region," in *Proceedings of IEEE Lasers and Electro-Optics Society Annual Meeting* (1994), **vol. 2** pp. 349–350.
20. G. Ghosh, "Dispersion-equation coefficients for the refractive index and birefringence of calcite and quartz crystals," *Opt. Commun.* **163**(1-3), 95–102 (1999).
21. A. D. Rakić, "Algorithm for the determination of intrinsic optical constants of metal films: application to aluminum," *Appl. Opt.* **34**(22), 4755–4767 (1995).
22. R. Zia, M. D. Selker, P. B. Catrysse, and M. L. Brongersma, "Geometries and materials for subwavelength surface plasmon modes," *J. Opt. Soc. Am. A* **21**(12), 2442–2446 (2004).
23. G. Veronis and S. Fan, "Modes of Subwavelength Plasmonic Slot Waveguides," *J. Lightwave Technol.* **25**(9), 2511–2521 (2007).
24. G. Veronis and S. Fan, "Guided subwavelength plasmonic mode supported by a slot in a thin metal film," *Opt. Lett.* **30**(24), 3359–3361 (2005).
25. A. Polyakov, M. Zolotarev, P. J. Schuck, and H. A. Padmore, "Collective behavior of impedance matched plasmonic nanocavities," *Opt. Express* **20**(7), 7685–7693 (2012).
26. A. Mizrahi, V. Lomakin, B. A. Slutsky, M. P. Nezhad, L. Feng, and Y. Fainman, "Low threshold gain metal coated laser nanoresonators," *Opt. Lett.* **33**(11), 1261–1263 (2008).
27. M. P. Nezhad, A. Simic, O. Bondarenko, B. Slutsky, A. Mizrahi, L. Feng, V. Lomakin, and Y. Fainman, "Room-temperature subwavelength metallo-dielectric lasers," *Nat. Photonics* **4**(6), 395–399 (2010).
28. K. Yu, A. Lakhani, and M. C. Wu, "Subwavelength metal-optic semiconductor nanopatch lasers," *Opt. Express* **18**(9), 8790–8799 (2010).
29. J. B. Lasky, "Wafer bonding for silicon-on-insulator technologies," *Appl. Phys. Lett.* **48**(1), 78-80 (1986).
30. C. C. Lee, G. S. Matijasevic, "Highly reliable die attachment on polished GaAs surfaces using gold-tin eutectic alloy," *IEEE T. Compon. Hybr.* **12**(3), 406-409, (1989)

1. Introduction

The continuous growth of Internet-related business has boosted the demand of high speed data transmission and low circuit power consumption. It is generally believed that a monolithic integration of silicon-based photonics and electronics might be a promising solution to those issues [1–12]. Yet, the indirect bandgap of silicon-based materials is always the biggest obstacle to be overcome in this integration platform [9, 10]. In the past decade, numerous methods have been proposed to obtain silicon-based lasers, such as Raman amplification [4], erbium-doped microdisks [5], nano-crystalline silicon structures [6], III-V/Si hybrid devices [7–12], and n-type strained Ge [13] etc. However, so far, the inefficiency of silicon light emission has not been solved yet.

Since its invention in 2006, the electrically-pumped hybrid III-V/silicon evanescent laser has become popular [8–12]. In this design, a III-V gain chip is directly bonded onto a passive silicon waveguide (WG) to form the resonant cavity of the device. Such laser can operate in continuous-wave output with a threshold current 65 mA, a maximum output power 1.8 mW with a differential quantum efficiency of 12.7% and a maximum operating temperature of 40 °C [8]. Besides, several device improvements in hybrid laser cavity designs [9], passive waveguide structure [10], epitaxial materials [11], and bonding process [12] have been demonstrated to achieve better performance than the prototype. Despite the impressive device performance of those demonstrations, the dimensions of the silicon waveguide in above devices are still much larger than the size that the photonic roadmap hopes to achieve in the future [14]. When there is request to reduce the dimensions of the underneath silicon waveguide to hundreds of nano-meters, this hybrid platform is prone to fail because the physical size of the waveguide can no longer support an optical mode. This effect can be easily demonstrated by finite element method (FEM) which will be the backbone of our simulation study. In the directly bonded III-V/silicon hybrid devices, when the cross-sectional

area of underneath silicon waveguide shrinks from $2.5\ \mu\text{m}$ by $0.76\ \mu\text{m}$ to $0.3\ \mu\text{m}$ by $0.76\ \mu\text{m}$, the optical field in the silicon section is greatly diminished, as shown in Fig. 1, and thus no optical power generated in III-V chip can be coupled into silicon when the silicon ridge goes sub-micron. Therefore, we propose a plasmonic hybrid III-V/Si evanescent laser, which combines the merits of optical gain of III-V chip and the small dimension of plasmonic waveguide, to achieve a feasible Si-based laser design in a nano-scale platform. From our simulation, the introduction of the periodic metal gratings can effectively modify the optical energy distribution in the structure and provide better confinement of the modes within the nano-meter scaled waveguide. The periodicity and the width of these gratings can be changed in normal semiconductor processes, and thus the coupling of the optical field can be engineered, which can be very important for the integration of nano-scaled III-V/silicon devices. In the following sections, a numerical study of such design will be performed, and general device dimensions and performance will be evaluated through simulations.

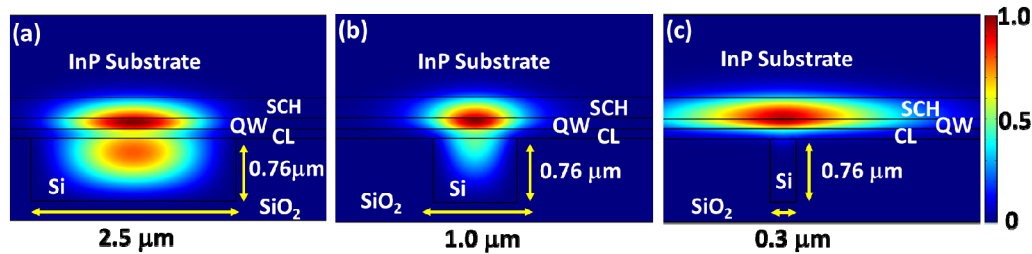


Fig. 1. The normalized energy density distributions for the directly bonded III-V/silicon device with (a) $2.5\ \mu\text{m}$ -, (b) $1.0\ \mu\text{m}$ - and (c) $0.3\ \mu\text{m}$ -wide silicon waveguide. All cases are calculated without metal grids in between III-V and silicon chips.

2. Proposed process flow

The basic schematic diagram of a proposed device is shown in Fig. 2(a). In order to accomplish this design, the process steps, as shown in Fig. 2(b), are suggested. First, we grow SiO_2 onto Si substrate and dry etch to form the groove. A thin aluminum (Al) layer was deposited in the groove to prevent optical energy from penetrating into the bulk substrate. Then, a plasma-enhanced chemical vapor deposition (PECVD) of silicon is performed to fill silicon material in the groove, forming silicon waveguide. After a suitable planarization process, such as chemical mechanical polishing (CMP), we utilize electron-beam (E-Beam) lithography to define the Al metal grating layer, dry etch again to form the periodic stripe pattern. Finally, a wafer bonding process is applied to combine III-V material with passive waveguide [8]. In the previous design, owing to different material thermal expansion coefficients [15], the trenches at the sides of silicon ridge waveguide [8] may develop stress during the wafer bonding process, presenting a higher risk to fail. Hence, we turn to the embedded ridge waveguide design to strengthen the finished structure. The nanoscale Al grating can be adjusted by E-beam process and the variations in period, width and depth will be important parameters for our device to success.

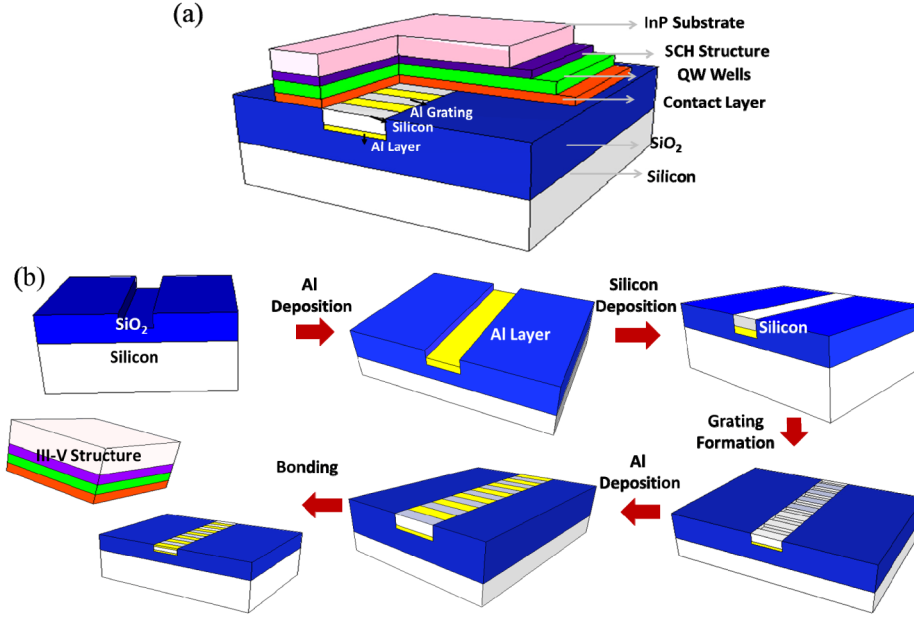


Fig. 2. The schematics of plasmonic hybrid III-V/Si evanescent lasers. (a) The final device (b) The proposed process flow.

3. Simulation methodology

To evaluate different design parameters such as grating period and waveguide height, we proceed a three-dimensional (3-D) eigenmode calculation at wavelength $1.55 \mu\text{m}$ by the finite-element method in COMSOL[®] differential equation solver. Both the cross-section and side views of the hybrid device are shown in Fig. 3. The coordinate system is also defined in the figure. The solver neglects the reflection from the boundaries in x and z directions, which are sometimes called scattering boundary condition [16]. In y direction, we choose the unit cell, as indicated by red dot lines in the Fig. 3(b), to be the calculation domain, and assume the periodic boundary condition in y -direction. Besides, the stability of the numerical results can be guaranteed by the convergence tests and be independent from mesh sizes and boundaries. The III-V structure, as shown in Fig. 3, consists of $1\text{-}\mu\text{m}$ InP substrate, $0.25\text{-}\mu\text{m}$ $\text{Al}_{0.131}\text{In}_{0.528}\text{Ga}_{0.34}\text{As}$ separated confinement hetero-structure (SCH), $0.125\text{-}\mu\text{m}$ $\text{Al}_{0.055}\text{In}_{0.653}\text{Ga}_{0.292}\text{As}$ quantum well (QW) and $0.12\text{-}\mu\text{m}$ InP contact layer. The height of the embedded silicon waveguide, H , can be treated as one of the variables, and the width of the waveguide is fixed at 300 nm ; the thickness of Al layer located at bottom of the silicon ridge waveguide is $0.05 \mu\text{m}$. The dimensions of metal gratings are h in depth, w in width and $0.1 \mu\text{m}$ in length and the periodicity is p (h , w , and p will be used as design variables in the following contents.). The refractive indices of materials used in the simulations are described in the Table 1. Other than the refractive index of Al, we only consider the real part of refractive index to observe the fundamental optical behaviors of the proposed device.

The optimization criterion is governed by the laser threshold gain of the device which is evaluated by [17]:

$$g_{th} = \frac{1}{\Gamma_{QW}} \times \left(\frac{n_{eff}(r)}{n_{QW}} \right) \times \left[\frac{4\pi n_{eff}(i)}{\lambda} + \frac{\ln(1/R^2)}{2\ell} \right] \quad (1)$$

where g_{th} is threshold gain, $n_{eff}(r)$ and $n_{eff}(i)$ is real part and imaginary part of effective index, respectively, λ is the target wavelength of $1.55 \mu\text{m}$, R is the reflectivity, Γ_{QW} is the power

confinement factor in quantum wells and n_{QW} is the refractive index equal to 3.6594. The cavity length in the y -direction, l , is deliberately set to be $30 \mu\text{m}$ in total. This reduced length, compared to $300 \mu\text{m}$ in most designs, is due to the everlasting request of scaling-down in the silicon IC industries, and also can be served as a testament for the potential of this hybrid platform. Note that we also assume the mirror loss is resulted from dielectric-air Fresnel reflection instead of from mirrors or any other reflectors, so R is $[(n_{\text{eff}}-1)/(n_{\text{eff}}+1)]^2$. The nature of this design brings us a large number of variables to deal with, including metal grating depth, width, and periods, silicon waveguide height etc. If all parameters are varying at the same time, the sheer quantity of calculation becomes impractical. So we assume that a global optimal g_{th} exists and no other significant saddle points for this solution. Under this assumption, we can focus on two or three variables at one time and optimize our design step by step with the g_{th} value winding down as the optimization procedure proceeds. We firstly determine the waveguide height (H) to have a well confined optical mode; then, the metal grating depth (h), width (w) and period (p) can be optimized subsequently. Low threshold gain (g_{th}) is usually preferred in a generic laser operation, however, we believe the transverse and longitudinal energy distribution patterns are also important for a good laser operation, and, thus, need to be considered.

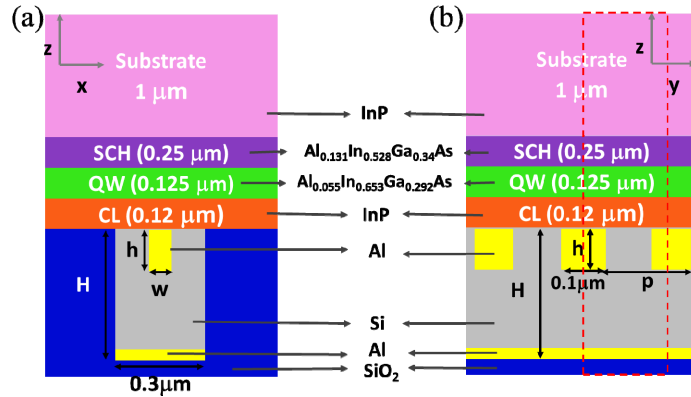


Fig. 3. The schematic of simulation models viewed from (a) the cross-section and (b) the side of the device.

Table 1. The refractive index of materials in simulation models

Material	Refractive Index
InP	3.1649 [18]
$\text{Al}_{0.131}\text{In}_{0.528}\text{Ga}_{0.34}\text{As}$	3.4907 [19]
$\text{Al}_{0.055}\text{In}_{0.653}\text{Ga}_{0.292}\text{As}$	3.6594 [19]
Si	3.477 [18]
SiO_2	1.5277 [20]
Al	$1.5785 + 15.658i$ [21]

4. Structural optimization of plasmonic III-V/silicon hybrid lasers

4.1 Mode behaviors with ridge height (H) and grating depth (h)

First the embedded ridge height (H) and Al grating depth (h) are set as variables to test their influences on the transverse energy distribution, and grating width (w) and period (p) are fixed at 0.1 and $0.3 \mu\text{m}$. The Fig. 4(a) and 4(b) show the real part and imaginary part of effective index with different ridge heights of 50 nm -, 100 nm - and 200 nm -deep Al gratings, respectively. From the simulation, the high real part is accompanied with the high imaginary

part of the effective refractive index. Besides, with increasing ridge height, the real part and imaginary part of effective indices reach stable values; the deeper the grating is, the lower asymptotical effective indices the devices get. Similar behaviors can be explained by the metal-insulator-metal model discussed previously [22–24]. Short distance between Al gratings and Al bottom layer results in stronger mutual coupling and high refractive index. However, as the distance between metal gratings and layer is gradually increased beyond a critical distance, the model shifts from metal-insulator-metal relation to the metal-insulator condition. In the meantime, the effective refractive index becomes constant and no longer correlates to the distance between top and bottom Al layer. Because this critical distance is a constant in our simulation, it is natural that the elbows of the refractive indices shifts like the red arrows in the Fig. 4 when Al grating depth is considered.

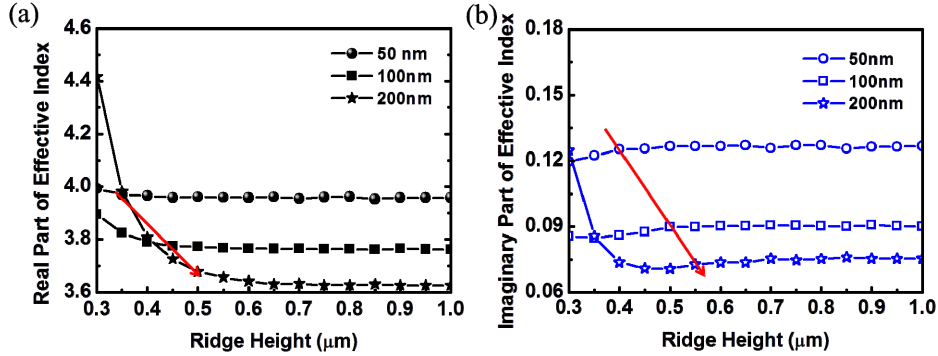


Fig. 4. (a) The real part and (b) imaginary part of effective refractive index of the device with different ridge height and Al grating depth. The inset shown in the (a) describes the definition of simulation parameters.

Figure 5(a) and 5(b) show the energy confinement factors of embedded ridge waveguide (Γ_{WG}) and quantum well structures (Γ_{QW}) with various ridge heights and grating depths, calculated by the equation:

$$\Gamma_{QW/WG} = \frac{\iiint_{QW/WG} |E|^2 dx dy dz}{\iiint_{Total} |E|^2 dx dy dz} \quad (2)$$

where E is electric field in the structure. In Fig. 5(a) and 5(b), the Γ_{WG} and Γ_{QW} oscillate periodically with the increasing ridge height. As shown in the inset of Fig. 5(b), the Γ_{WG} and Γ_{QW} are complementary to each other under the same Al grating depth. When Al grating depth increases, the waveguide confinement (Γ_{WG}) tends to increase while the Γ_{QW} goes down as shown in Fig. 5(a) and 5(b). This tendency indicates that as the top Al layer grows thicker, the optical energy resides more easily in the waveguide part, not the upper quantum well region. Besides, the calculated threshold gain is shown in the Fig. 5(c). Even though most points of threshold gains are located around $20 \mu\text{m}^{-1}$, not every condition is suitable for our device. In fact, with increasing ridge height, more propagating modes can exist along the waveguide. However, multi-modes are unfavorable to the laser device most of time. Hence, we can't determine the parameters only through the threshold data, but also take the energy distribution into consideration. Figure 5(d) is the cross-section view of our structure, and from Fig. 5(e) to 5(g), the normalized energy density distributions of different ridge heights (Fig. 5(e): $0.3 \mu\text{m}$, Fig. 5(f): $0.6 \mu\text{m}$, Fig. 5(g): $0.9 \mu\text{m}$) are shown. The energy density is calculated by $(1/2) \times \text{Re}[E \times H^*]$ and normalized to its maximum value in each case. Figure 5(e)-5(g) describe how the energy density distribution evolves when the ridge height changes. As the height of buried silicon waveguide is increased from 0.3 to $0.9 \mu\text{m}$, transformation in energy distribution is expected. With small waveguide height, only the surface plasmonic polariton (SPP) mode on the bottom Al layer is possible (like in $0.3 \mu\text{m}$ case of Fig. 5(e)). However, if

the ridge is too high, as in Fig. 5(g), multiple transverse hybrid SPP modes can be seen in the waveguide. We believe if the design falls in the middle of these two situations, it will be the best for the lasers device (as in Fig. 5(f)).

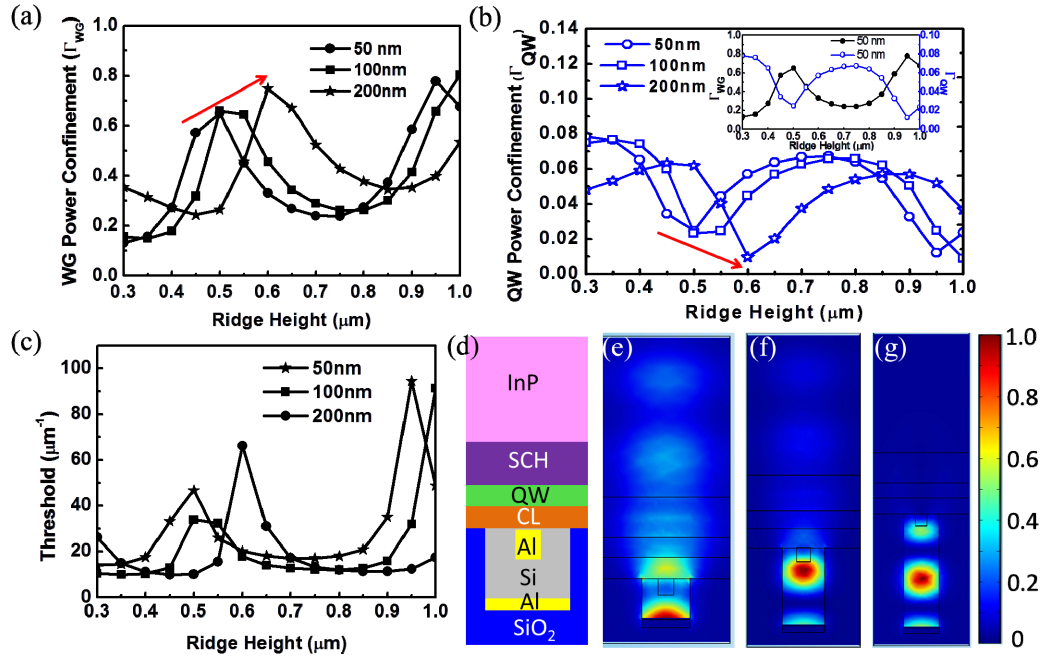


Fig. 5. (a) The silicon waveguide (WG) and (b) the quantum well (QW) power confinement with various ridge heights and Al grating depths. (c) the calculated threshold gain of the device. (d) the corresponding structure schematic to the simulated normalized energy density distribution results with (e) 0.3 μm -, (f) 0.6 μm - and (g) 0.9 μm -high ridge.

4.2 Mode behaviors with grating depth (h) and grating width (w)

Using the information from previous section, the ridge height is fixed at 0.6 μm to ensure there is only one guided mode supported in the waveguide. Figure 6(a) shows the real part and imaginary part of refractive indices with different Al metal grating depth (h), and width (w). Similar to Fig. 4, the behavior of real effective index is positively correlated with the imaginary one. In shallow grating depth region, the metal-metal coupling is weak. For deeper grating, the effective indices would go down. After the critical depth of the grating is reached, like the critical ridge height discussed in previous section, the indices soar dramatically before the grating is attached to bottom Al layer, because of stronger metal-metal coupling [23, 24]. However, once two metals are connected together at grating depth 0.55 μm , the effective indices suddenly drop to the low value, indicating the system has been changed to a simple case of III-V based waveguide and the optical energy is tightly confined in the InP-based region as shown in Fig. 6(g). Connected metals also cause the rebound of the power confinement Γ_{QW} with a higher loss due to larger metal portion in the cross-section, as shown in the Fig. 6(b). Nevertheless, even though increasing the grating width slightly lowers the effective indices, it doesn't change the trend of effective indices with grating depth.

The threshold gain is also calculated to determine suitable parameters of metal grating depth (h) and width (w) in our design, as shown in the Fig. 6(c). Between 0.3 μm - and 0.5 μm -deep metal gratings, because of very few confined energy in the QW, the calculated threshold soars high; conversely, the extremely low threshold occurs at the grating width 0.3 μm and depth in the range from 0.05 μm to 0.25 μm .

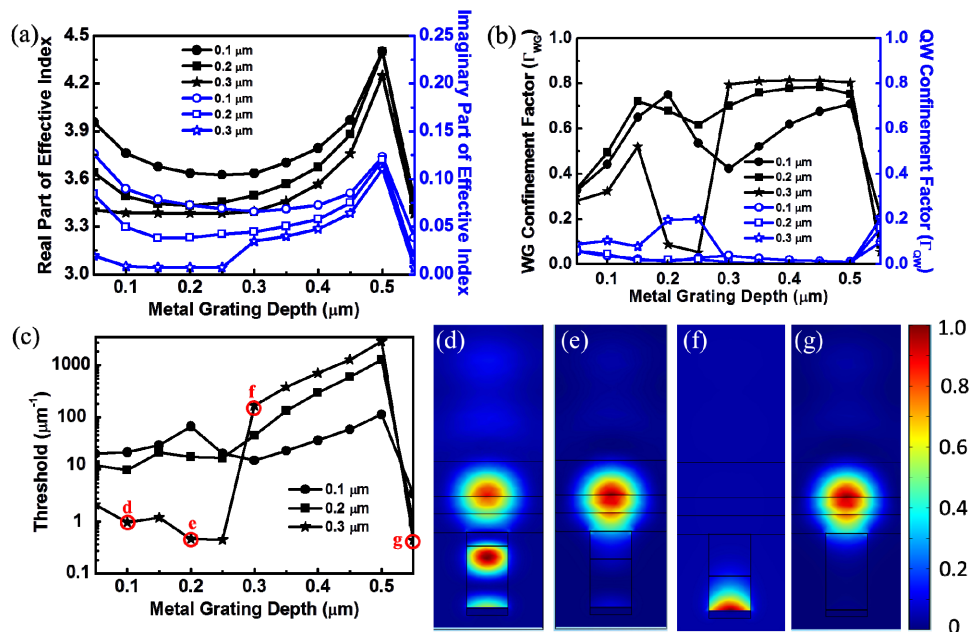


Fig. 6. (a) The real part and imaginary part of effective refractive index with various Al grating depths and widths. Different widths of Al gratings (0.1, 0.2 or 0.3 μm) do not change the shape of the curve, only the relative magnitude of refractive indices. (b) The silicon waveguide (in black color) and the quantum well (in blue color) power confinement. (c) the calculated threshold gain of the device. (d)-(g): the normalized energy density distributions of the device with different grating depths: (d) 0.1 μm-, (e) 0.2 μm-, (f) 0.3 μm-, and (g) 0.55 μm. The corresponding g_{th} is marked in Fig. 6(c).

Figure 6(d) to 6(g) show the energy density distribution of devices with 0.3 μm metal grating width and various grating depths. When the grating depth (or the metal depth) is thin, the optical energy distribution can be divided into two groups: one in the III-V section and the other coupled to metal layer in the silicon waveguide. Once the metal thickness increases, the optical energy could be confined either in the QW region or in the silicon waveguide region as shown in Fig. 6(e) or in Fig. 6(f). Finally, when metal grating is too thick, touching the bottom Al layer, any modes in the bottom silicon waveguide are virtually extinguished; i.e., only modes in the III-V section can propagate as shown in Fig. 6(g). Besides, grating width doesn't alternate the trends of the effective indices of the structure (in Fig. 6(a)); however, it does move the dip of the confinement factor around like in Fig. 6(b). This behavior is almost like the sub-wavelength gratings [25] which can form a resonant cavity effect. Despite low threshold gains occur at these parameters, as labeled in the Fig. 6(c), we believe only the device with 0.1 μm grating depth is suitable for our device design because of equally energy distribution in QW and waveguide structures so that the light can transmit in the waveguide and replenish the energy from the QW gain medium, simultaneously.

4.3 Mode behaviors with grating period (p)

After the cross-section geometry of the hybrid device is considered, there is still one dimension left undetermined: periodicity of the gratings in the y-direction. The effective indices are insensitive to the changes of periodicity, and only fluctuating around the effective index value at 3.387-0.0085i. However, for the Γ_{WG} and Γ_{QW} , depicted in the Fig. 7(a), the power distribution is periodically oscillating with metal grating period. Similar to the previous discussion in Fig. 5 and Fig. 6, Γ_{WG} and Γ_{QW} are complementary to each other when

the period of grating varies. With closer inspection, the characteristic curve repeats its pattern every 550 nm, like Γ_{WG} shown in the Fig. 7(a). In addition, every cycle in the Fig. 7(a) is composed of three parts: 1. Strong spike, 2. shoulder, and 3. small pike. For long period of gratings, more energy is transferred from waveguide to quantum well structure; consequently, the strong spike becomes weaker and broader, leading to smoother profiles. The energy shift with increasing period can also be observed in the normalized energy density distribution in Fig. 7(c)-7(h). We label three maximum points of characteristic waves in the first two cycles, as indicated in the Fig. 7(b), to compare the energy density distribution between cycle 1 and cycle 2. The energy density distribution for the structure in the cycle 1 (Fig. 7(c)-7(e)) is similar to that in the cycle 2 (Fig. 7(f)-7(h)), but with more energy in the QW than in the WG region. Therefore, the device with longer period of gratings can be with lower threshold gain owing to more energy located in the gain medium, as shown in the Fig. 7(b). The behavior of threshold gain period is quite similar to that of confinement factor in the Fig. 7(a) from the Eq. (1). With the considerations of lower gain threshold, optical modes in the waveguide and the tolerance in fabrication error, we believe the better period range should be designated from 2 μm to 3 μm , where the curve is comparatively flat. But if the overall dimension is limited, sub-micron design (like in case Fig. 7(e)) is also possible. Most importantly, the gain threshold is about $0.6 \mu\text{m}^{-1}$.

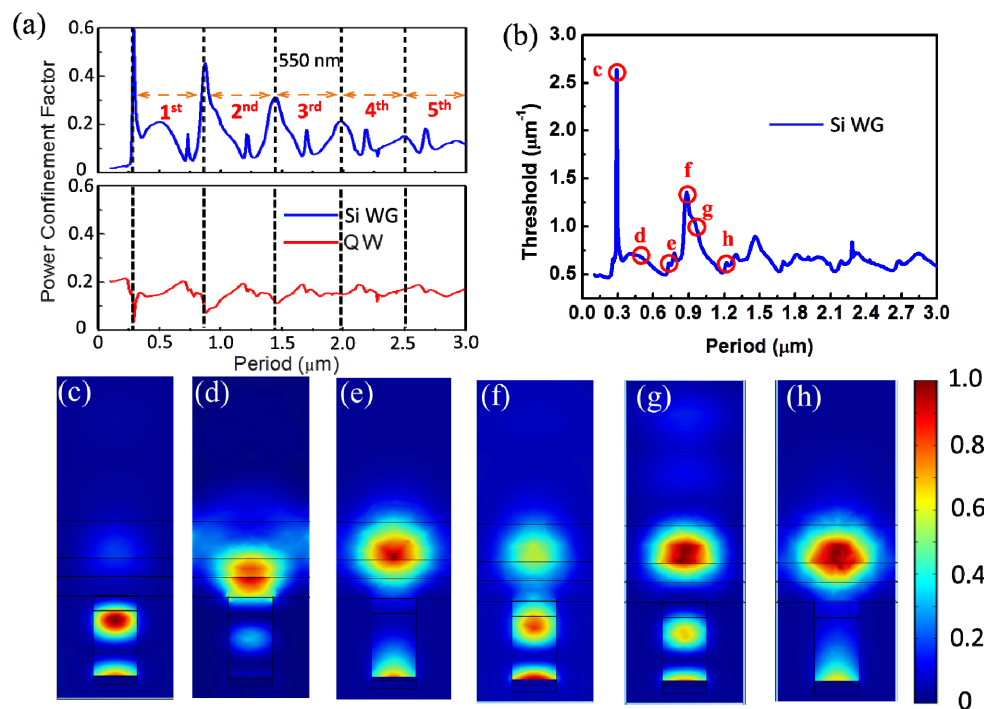


Fig. 7. (a) The silicon waveguide (WG) and the quantum well (QW) power confinement factor of the device with period from 0.1 μm to 3 μm . (b) the calculated threshold gain of the device. The corresponding normalized energy density distribution with the grating period at (c) 0.29 μm , (d) 0.5 μm , (e) 0.73 μm , (f) 0.87 μm , (g) 0.93 μm and (h) 1.21 μm , which are labeled in the (b) via red circles.

In the past, a nano-scale laser can usually yield ultra-low threshold gain (from tens to several hundreds of cm^{-1} [26–28]) during operation. Our design, on the other hand, is the traditional quantum well with micron-scale length of the active region. While the theoretical calculation and the past data [17] predict the proposed structure is possible for an electrically pumped laser, it has to be pointed out that this design sacrifices the performance due to a

smaller active region and extra loss from metal gratings in order to achieve the higher yield in metal bonding process [29, 30] and better optical mode coupling into silicon waveguide. The final optimized structure parameters are listed in Table 2.

Table 2. Optimized structural parameters of a nano-scale plasmonic hybrid laser

Ridge Height (H)	Ridge Width	Metal Depth (h)	Metal Width (w)	Metal Length	Period (P)
600	300	100	300	100	730

All units are in nm, the QW power confinement factor is 16.3%, and threshold gain is $0.616 \mu\text{m}^{-1}$.

5. Conclusion

In conclusion, we propose an alternative method to fabricate a small-sized hybrid III-V/Silicon laser device, whose device length is dramatically reduced from $300 \mu\text{m}$ to $30 \mu\text{m}$ with integrated metal grating layers. The simulation software also assists us to determine the favorable fabrication parameters including ridge height for $0.6 \mu\text{m}$, Al grating width and depth at $0.3 \mu\text{m}$ and $0.1 \mu\text{m}$, respectively. The grating period can be as small as 730 nm although 2 to $3 \mu\text{m}$ would be better in terms of process tolerance. Most of all, the calculated gain threshold, around $0.6 \mu\text{m}^{-1}$, shows great potential to realize this design in practice.

Acknowledgments

The authors would like to thank the technical supports of COMSOL from Prof. Tien-Chang Lu and Prof. Peichen Yu of National Chiao Tung University. This work is sponsored by National Science Council of Taiwan through the contract numbers of NSC 99-2221-E-009-052-MY3, NSC 102-2120-M-110-005 and NSC 102-3113-E-005-001.